AGU100 ADVANCING EARTH AND SPACE SCIENCE

Geophysical Research Letters

RESEARCH LETTER
10.1029/2018GL080492

Key Points:
- Our 3-m long granite experiment generates fully and partially confined stick-slip events
- Termination of lab earthquakes is well described by a fracture mechanics-based model with one free parameter: fracture energy coefficient
- Friction is similar enough between PMMA and rock, for termination studies

Supporting Information:
- Supporting Information S1

Correspondence to:
G. C. McLaskey,
gcm8@cornell.edu

Citation:
Ke, C.-Y., McLaskey, G. C., & Kammer, D. S. (2018). Rupture termination in laboratory-generated earthquakes. *Geophysical Research Letters*, *45*. https://doi.org/10.1029/2018GL080492

Received 14 SEP 2018
Accepted 21 NOV 2018
Accepted article online 28 NOV 2018

Rupture Termination in Laboratory-Generated Earthquakes

Chun-Yu Ke[1], **Gregory C. McLaskey**[1], **and David S. Kammer**[1]

[1] School of Civil and Environmental Engineering, Cornell University, Ithaca, NY, USA

Abstract Earthquakes are dynamic rupture events that initiate, propagate, and terminate on faults within the Earth's crust. Understanding rupture termination is essential for accurately estimating the maximum magnitude earthquake a region might experience. We study termination on sequences of **M** −2.5 earthquakes that rupture a 3-m granite laboratory sample. At this large scale, nucleation, propagation, and termination are either completely or partially confined within the sample – unique observations for experiments on rock. We compare measured termination locations to estimates from a fracture mechanics-based model to quantify the fracture energy of the laboratory earthquakes, which compare well with estimates from small natural quakes. Our results provide a mathematical framework that links micrometer-scale friction parameters to meter-scale earthquake mechanics, shows that a 3-m slab of granite can behave similar to a 200-mm sheet of glassy polymer, and demonstrates how small events can prime a fault for larger, damaging ones.

Plain Language Summary We have built a machine that squeezes a 3-m long slab of granite to generate sequences of slip events that spontaneously rupture a precut planar fault within the rock, similar to how earthquakes rupture faults within the Earth. While slip events generated on most rock mechanics machines rupture through the entire sample, the slip events we generate at this large scale are more realistic of natural earthquakes because rupture often stops after propagating only part-way down the rock sample. We describe a model that allows us to quantify where and why a rupture stops as a function of the stress distribution on the fault and friction properties. By matching the model to the experiment we estimate the fault's fracture energy. The model can also be used to show how small earthquakes can prepare a fault for a larger one.

1. Introduction

Physics-based earthquake models are increasingly used to study fault rupture propagation and seismic radiation (Harris et al., 2009). Direct field measurement of relevant fault properties such as stress state and friction remains mostly inaccessible, so laboratory experiments are employed to provide insight. For example, friction equations commonly used in earthquake simulations are based on laboratory experiments (Marone, 1998) conducted on ~100-mm-sized samples (Dieterich, 1979) at sliding velocities of ~1 μm/s up to 1 m/s (Di Toro et al., 2011). A different set of experiments focuses on fault rupture propagation (Mclaskey & Yamashita, 2017; Passelegue et al., 2013; Rubinstein et al., 2004; Xia et al., 2005) where the simulated fault remains essentially locked (slip rates <10 nm/s) before sudden episodes of unstable sliding (>0.1 m/s) that radiate seismically. Though challenging to interpret, these stick-slip events more accurately reflect the earthquake cycle, where crustal rocks undergo long stationary healing phases punctuated by dynamic ruptures that introduce slip accelerations in excess of 20 km/s^2 (Chang et al., 2012; McLaskey et al., 2015). Stick-slip experiments that rupture the entire sample are common, but more realistic events that are confined within a sample, as schematically shown in Figure 1a, are difficult to achieve in a lab. First, the sample must be large enough for dynamic slip events to nucleate from within the rock mass independent of the loading apparatus (Mclaskey & Yamashita, 2017). Second, fault conditions must be heterogeneous enough to stop the rupture before it reaches the sample boundaries. Confined ruptures on rock have thus far only been achieved on a 2-m sample by using fluid injection to set up favorable stress heterogeneity (Lockner et al., 1982). Confined rupture events have also been possible on more compliant materials such as glassy polymers (Bayart et al., 2016; Ben-David et al., 2010; Maegawa et al., 2010; Rubinstein et al., 2007), assumed to be an adequate analog for crustal rocks (Xia et al., 2005). We have developed an experiment on rock that is both large in scale and supports heterogeneous along-fault stress distributions. These conditions generate sequences of dynamic slip events that

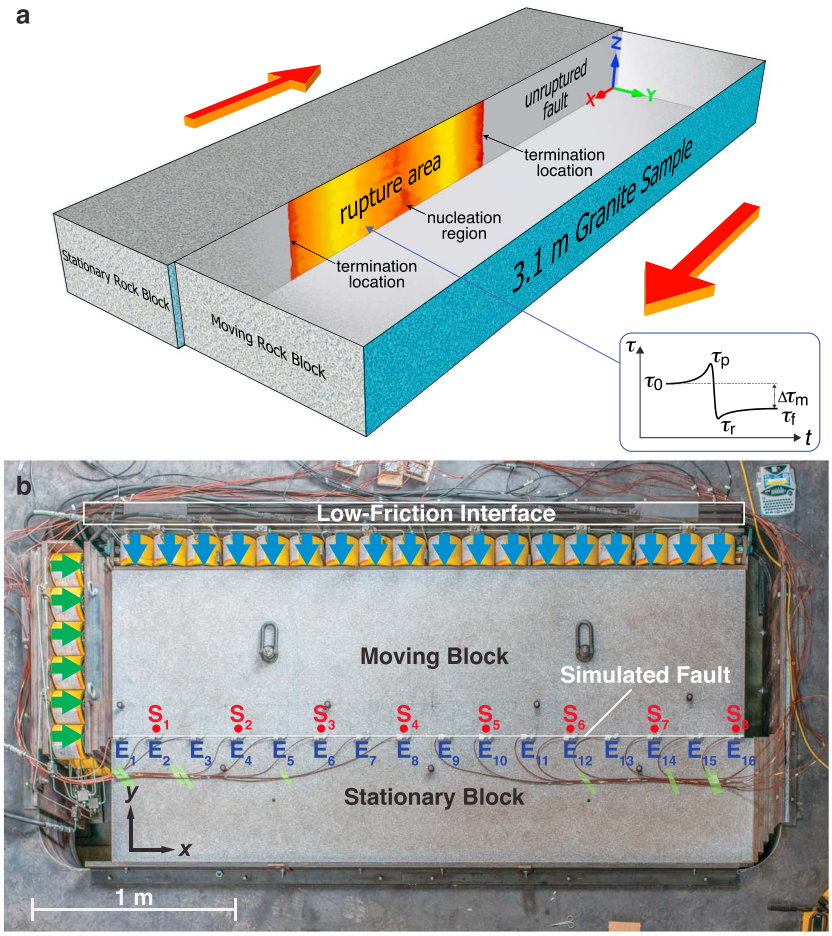

Figure 1. Three-meter laboratory earthquake. (a) Schematic illustration of a fully contained laboratory earthquake rupturing the interface between two granite blocks. Slip events nucleate and arrest before reaching the edge of the sample. (inset) Schematic evolution of stress at a representative point inside the rupture area. (b) Annotated photograph of the sample and loading apparatus. Two 3-m long granite blocks are placed in a 4.9 × 3.0 m steel frame. Loaded biaxially with 54 hydraulic cylinders, the moving block translates in the $+x$ direction, and deformation is accommodated on both the simulated fault and a low-friction bearing interface. Slip sensors (E_1 –E_{16}) are evenly spaced along the 3-m long fault. Strain rosettes (S_1 –S_8) are collocated with even-numbered slip sensors, glued $y \approx 7$ mm away from the simulated fault on the moving block.

can switch between smaller confined events and larger ones that rupture the entire sample. This gives us the opportunity to understand the conditions that lead to rupture termination. Here we utilize a linear elastic fracture mechanics-based model as a framework that links stress conditions and friction properties to rupture length and allows us to estimate the fracture energy of the granite fault.

2. Methods

2.1. Experimental System

The biaxial loading apparatus, shown in Figure 1b, applies normal stress σ and shear stress τ on a simulated fault that is the interface between two Barre Gray granite blocks. The normal loading array consists of 18 × 2 connected hydraulic cylinders and presses the two blocks together in the y direction. The shear loading array consists of 6 × 3 connected hydraulic cylinders and pushes the moving block in the $+x$ direction with respect to the stationary block. These hydraulic cylinders apply forces to the sample through loading platens composed of steel plates. The two arrays are connected to separate pumps, and their measured hydraulic pressure was used to calculate sample-average normal stress $\bar{\sigma}$ and shear stress $\bar{\tau}$ on the simulated fault. A low-friction interface composed of a 2.4-mm thick sheet of reinforced Teflon sliding on precision ground steel ($\mu = \tau/\sigma \approx 0.1$) allows the normal loading array to translate with the moving block in the x direction.

The dimensions of the moving block and the stationary block are $3.10 \times 0.81 \times 0.30$ and $3.15 \times 0.61 \times 0.30$ m (respectively) in the x, y, and z directions. The interface between two granite blocks is the 3.1-m long 0.3-m wide simulated fault with area $A = 0.95\ \mathrm{m}^2$. The fault surfaces of the granite samples were prepared by the manufacturer to be flat and parallel to 125 μm. In a "run in" operation performed before the experiments, the sample was forced to slip 20 mm at $\bar{\sigma} \approx 7$ MPa. During this period, the interface strengthened, slip events became larger and more abrupt, and a ~10-μm thick gouge layer formed. Additional experimental details can be found in Mclaskey and Yamashita (2017), which describes a one-fourth scale experimental replica with similar instrumentation.

2.2. Experimental Measurements

The displacement between two blocks along the simulated fault was measured by 16 eddy current sensors ($E_1 - E_{16}$) evenly spaced along the length of the fault, as shown in Figure 1b, and recorded at 50 kHz then averaged to 5 kHz to reduce high-frequency noise. Strain was measured by eight strain gage rosettes collocated with even-numbered eddy current sensors and recorded at 100 Hz. Each rosette consists of three collocated 5-mm-long strain gages oriented at 45°, 90°, and 135° from the fault which were glued to the moving block, 7 mm from the fault. Local stresses σ_{xx}, σ_{yy}, and σ_{xy} were derived from the three independent components of the 2-D strain tensor measured from the strain rosette and elastic properties of Barre Gray granite, static Young's modulus $E_\infty = 30$ GPa, and Poisson's ratio $\nu = 0.23$, where $\sigma \equiv -\sigma_{yy}$ and $\tau \equiv \sigma_{xy}$.

2.3. Experimental Procedure

In typical experiments, normal stress was set to a prescribed level ($\bar{\sigma}_0$ =1 – 10 MPa) and was kept approximately constant. Shear stress was then increased at a roughly constant rate ($\dot{\bar{\tau}} = 0.01$ MPa/s) to induce slip events. This procedure produces sequences of regular, periodic stick-slip events that rupture the entire simulated fault, yet occasional changes of prescribed $\bar{\sigma}_0$ create inhomogeneous distributions of $\sigma(x)$ and/or $\tau(x)$ (Figure 3a) that support sequences of confined slip events. For example, when $\bar{\sigma}$ was increased from 1 to 4 MPa, we observed sequences of bilateral confined slip events that nucleated at $x \approx 2$ m (Figure 2b). In contrast, more modest increases of $\bar{\sigma}$ from 7 to 8 MPa (Figure 2a), and decreases in $\bar{\sigma}$ (Figure S1) caused sequences of unilateral confined slip events which nucleated at $x \approx 0 - 1$ m, similar to observations on smaller poly(methyl methacrylate) (PMMA) samples (Maegawa et al., 2010; Rubinstein et al., 2007). Interestingly, confined slip events occasionally occur between complete ruptures (e.g., event iv in Figure 2a), similar to how natural earthquakes vary in size.

The inhomogeneous stress distributions that are set up by the loading procedures outlined above are essential for making the confined rupture events (Figure 3 top panels). For example, events I–III in Figure 2b nucleated near $x = 2$ m because that is the location on the fault where $\tau_0(x)/\sigma_0(x)$ is maximal (Figure 3a). Furthermore, $\tau_0(x)/\sigma_0(x)$ cannot be uniform; otherwise rupture will propagate through the entire fault. The nonuniform stress distribution results from the compliance of the steel loading frame, net moment from the shear loading cylinders, and sample edge effects. $\tau_0(x)$ and $\sigma_0(x)$ were qualitatively verified by finite element analysis (Figure S2). Note that $\bar{\sigma}$ on the simulated fault is coupled to shear stress $\bar{\tau}$ through frustrated Poisson expansion due to the confinement of the loading apparatus in both x and y direction, that is, $\int_0^L \sigma(x)dx = \int_0^L \sigma_0(x)dx + C\int_0^L \tau(x)dx$, where L is the length of the simulated fault and $C \approx 0.1$.

3. Experimental Observations

When slip events initiate, the slipping patch size must exceed a critical dimension before it rapidly accelerates (reaching ≈2,300 m/s) and radiates the seismic waves characteristic of standard earthquakes (Ampuero & Rubin, 2008; Uenishi & Rice, 2003). We observed a ~0.5 m critical dimension, and this appears to control the minimum event magnitude. The rupture lengths of fully confined slip events, for example, events I and II in Figure 2, ranged from 0.8 to 1.8 m, slip measured near the center of the ruptured region ranged from 10 to 20 μm, and corresponding magnitudes ranged from **M** −2.8 to **M** −2.4. Reported event magnitudes were determined from seismic moment $M_0 = GAD$, estimated from average fault slip D, the shear modulus G of the rock and rupture area A. Slip was assumed to be uniform through the 0.3-m thickness of the granite slab; measurements from slip sensors placed on the bottom surface of the slab for some experiments supported this assumption. Maximum recorded slip velocity was around 20 – 100 mm/s and slip accelerations were at least 35 – 180 m/s^2. Note that higher local slip velocity and acceleration (20 km/s^2) is expected to be resolvable when higher frequency motion is recorded (McLaskey et al., 2015), but our slip sensors only detect frequencies $f \leq 5$ kHz. The confined slip events are more similar to real earthquakes than complete-rupture "stick-slip"

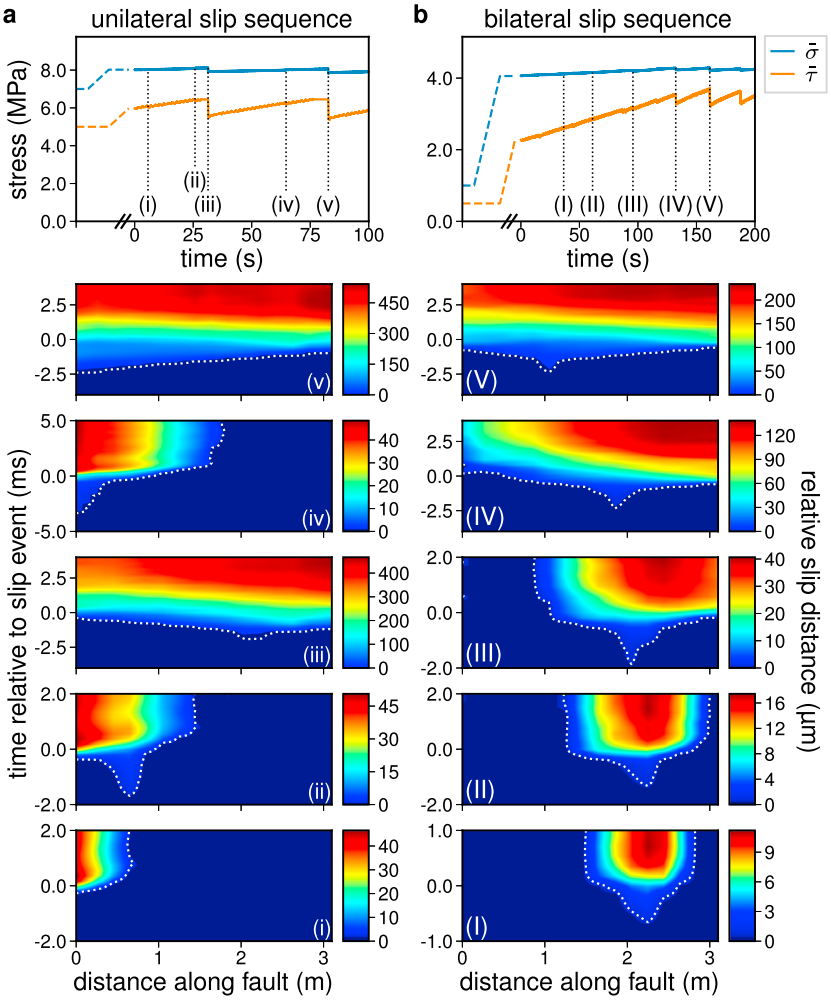

Figure 2. A sequence of (a) unilateral and (b) bilateral confined slip events. (top) Sample-averaged normal $\bar{\sigma}$ and shear $\bar{\tau}$ stress as a function of time. Initial loading is schematically depicted by dashed curves. The slip instabilities are numbered and marked by dotted lines. (bottom) Space-time plots of relative slip distance during the slip events marked in (top). Color bars change for each slip event. The transition from sticking to sliding is highlighted by dotted white line to emphasize rupture nucleation and termination.

events, for example, events v and V in Figure 2, because fault slip increases with increasing rupture length and the rupture is completely confined within the rock sample.

Since the confined slip events are similar to earthquakes, we study how their rupture termination is related to the fault stress distribution and friction properties. When a slip event propagates past a point on the fault, stress increases from initial stress level τ_0 to peak frictional strength τ_p and then drops toward the residual frictional strength τ_r before ending at the final stress level τ_f (Figure 1, inset). We measure τ_0 and τ_f just prior to and after dynamic slip events, respectively, and calculate $\Delta\tau_m(x) = \tau_0(x) - \tau_f(x)$. In general, stress drops ($\Delta\tau_m > 0$) within the center of the ruptured region and increases ($\Delta\tau_m < 0$) near the arrest locations (Figure 3b).

4. Theoretical Model

We consider slip fronts as mode-II cracks in the linear elastic fracture mechanics (LEFM) framework (Bayart et al., 2016, 2018; Kammer et al., 2015; Svetlizky & Fineberg, 2014). The conditions for rupture are a competition between the dynamic energy release rate G^d_{II}, that fuels the rupture, and fracture energy Γ consumed by unit rupture advance. During the propagation of an earthquake rupture $G^d_{II} = \Gamma$ (Freund, 1979; Svetlizky et al., 2017). Rupture terminates when it reaches a barrier (higher Γ) or runs out of available strain energy (lower G^d_{II}). G^d_{II} depends on the rupture speed and is, for time-independent loading, maximal at rest

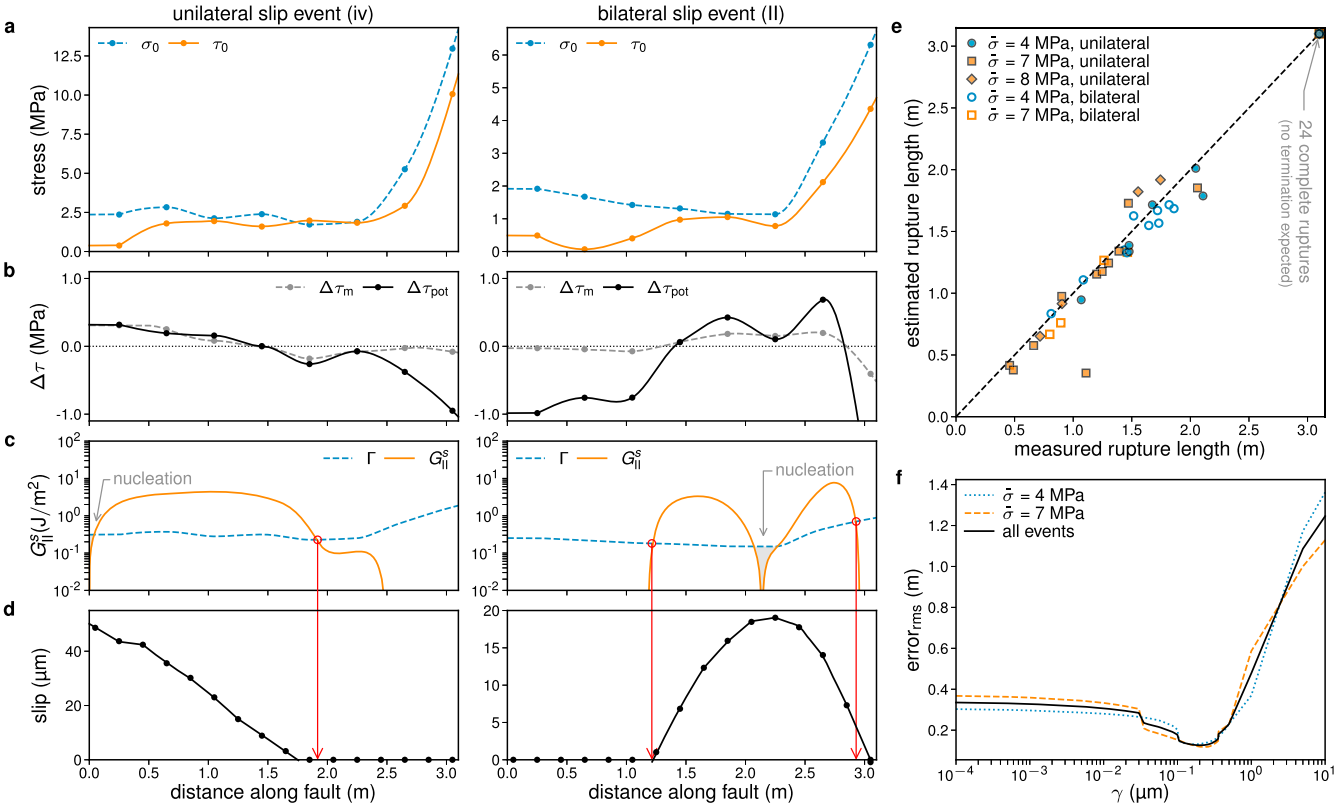

Figure 3. Mechanics of dynamic rupture termination and comparison to linear elastic fracture mechanics estimates. Representative examples of unilateral and bilateral confined slip events are shown in the left and right columns, respectively. (a) Normal stress $\sigma_0(x)$ and shear stress $\tau_0(x)$ measured before slip event. (b) Measured stress change $\Delta\tau_m(x) = \tau_0(x) - \tau_f(x)$ and estimated potential stress drop $\Delta\tau_{pot}(x) = \tau_0(x) - \tau_r(x)$ (equation (5)). (c) Following equation (1), static energy release rate $G^s_{II}(x)$ (equation (2)) is compared to fracture energy $\Gamma(x)$ (equation (7)) to determine rupture termination location (red circle), where $G^s_{II}(x) = \Gamma(x)$. $G^s_{II}(x)$ is computed from $\Delta\tau_{pot}(x)$ and $\Gamma(x) = \gamma\sigma_0(x)$, where γ is the fracture energy coefficient and is the one free parameter in the model. The unilateral and bilateral ruptures nucleate at $x \approx 0$ m and $x \approx 2.2$ m, respectively. (d) Fault slip distribution from measurements at 16 locations (E_1 –E_{16}). (e) Comparison of estimated and measured rupture lengths for 21 unilateral, 14 bilateral confined, and 24 complete ruptures, listed in Table S1. Linear elastic fracture mechanics estimates of rupture length are based on $\gamma = 0.2$ μm. (f) Root-mean-square error of rupture length estimation of all confined slip events as a function of γ (black curve). Separate curves are shown for subsets of slip events at $\bar{\sigma} = 4$ MPa (blue dotted) and $\bar{\sigma} = 7$ MPa (orange dashed).

$G^s_{II} = G^d_{II}(v = 0) \geq G^d_{II}(v > 0)$. Thus, the static energy release rate G^s_{II} provides a rupture arrest criterion through

$$G^s_{II}(x) = \Gamma(x), \tag{1}$$

where x is the crack tip position. While $\Gamma(x)$ is a local property of the interface, $G^s_{II}(x)$ depends on the spatial extent of the rupture and is nonlocal. $G^s_{II}(x)$ is related to the mode-II static stress intensity factor $K^s_{II}(x)$ by

$$G^s_{II} = \frac{\alpha}{E_0}(K^s_{II})^2, \tag{2}$$

where $\alpha = 1$ for plane stress assumption and E_0 is the instantaneous elastic modulus. K^s_{II} can be computed at a crack tip position x through $x = x_c \pm a$ with x_c being the center of the crack and known equations that express the stress intensity factor as a function of crack half-length a. We approximate K^s_{II} for (semi-)infinite solids by employing Equations 5.10 and 8.3 in Tada et al. (2000), where for an edge crack in a semi-infinite solid,

$$K^s_{II}(a) = \frac{2}{\sqrt{\pi a}} \int_0^a \Delta\tau_{pot}(s) \frac{F(s/a)}{\sqrt{1 - s/a)^2}} ds, \tag{3}$$

with $F(s/a) = 1.297 - 0.297(s/a)^{5/4}$ and $x_c = 0$, and for a bilateral crack in an infinite solid,

$$K^s_{II}(x_c \pm a) = \frac{1}{\sqrt{\pi a}} \int_{-a}^a \Delta\tau_{pot}(x_c + s) \sqrt{\frac{a \pm s}{a \mp s}} ds. \tag{4}$$

More details on solving rupture termination for bilateral events is given in Text S1. The potential stress change along the simulated fault is given by

$$\Delta\tau_{pot}(x) = \tau_0(x) - \tau_r(x), \tag{5}$$

which depends on the measured shear stress before the slip event $\tau_0(x)$, and the residual shear stress $\tau_r(x)$ (equation (6)). Note that $\Delta\tau_{pot}(x) \approx \Delta\tau_m(x)$ within the ruptured region, whereas $\Delta\tau_{pot}(x) \neq \Delta\tau_m(x)$ otherwise, because no slip occurs that releases stress.

Applying LEFM theory to predict the extent of a rupture would require beforehand knowledge of $\Delta\tau_{pot}(x)$. While $\tau_0(x)$ is measured, $\tau_r(x)$ is the residual friction force and depends on the exact friction law, which is currently unknown. We therefore used measured post event shear stresses $\tau_f(x)$ from a subsequent complete rupture to estimate $\tau_r(x)$ over the entire length of the fault. If we assumed $\tau_r(x) = \tau_f(x)$ of the confined event, rupture would be artificially limited by the measured stress increases near the arrest location, which is not residual friction but redistributed stress, and would not allow us to determine whether the rupture could have propagated further. Precisely, we estimated $\tau_r(x)$ of a confined slip event by scaling a measured reference stress distribution $\tau_f^{ref}(x)$ to the current sample-average stress level through

$$\tau_r(x) = R\tau_f^{ref}(x), \tag{6}$$

where R is a scale factor that equates $\tau_f(x)$ in the fault section that was ruptured in both events such that $R = \int_{x_l}^{x_r} \tau_f(x)dx \Big/ \int_{x_l}^{x_r} \tau_f^{ref}(x)dx$. We define $\tau_f^{ref}(x)$ to be the $\tau_f(x)$ measured after the second consecutive complete rupture event of each sequence. Since $\tau_f(x)$ is measured after a dynamic response of the rock, we use dynamic elastic properties of the granite to compute stress from strain measurements by following $\tau_f(x) = [E_\infty\epsilon_{xy}^0(x) + E_0(\epsilon_{xy}^f(x) - \epsilon_{xy}^0(x))]/(1+\nu)$, where $E_\infty\epsilon_{xy}^0(x) = \tau_0(x)$ is the prestress distribution and $\epsilon_{xy}^f(x)$ the strain measurement after the rupture event. The instantaneous elastic modulus $E_0 = 44.5$ GPa, estimated from wave speed measurements, is larger than the static $E_\infty = 30$ GPa. It is important to note that through this approach, we assume that $\tau_r(x) \approx \tau_f(x)$ within the ruptured region, and thus make no distinction between static and dynamic stress drop. This assumption should be valid for the crack-like events observed here (Viesca & Garagash, 2015).

Following previous studies (Bayart et al., 2016; Kammer et al., 2015), we assume fracture energy is directly proportional to normal stress and formulate

$$\Gamma(x) = \gamma\sigma_0(x), \tag{7}$$

where γ is the fracture energy coefficient considered here to be constant. γ is the only free parameter in our model and is determined by comparing measured and LEFM-estimated rupture lengths for 35 confined slip events, shown in Figure 3e. The root-mean-square of the errors was minimized to determine 0.03 μm $< \gamma <$ 0.5 μm, with a preferred value of 0.2 μm (Figure 3f). In Figure 3c, we compare $G_{II}^s(x)$ and $\Gamma(x)$ to estimate the rupture termination location. Starting from the location of nucleation, $\Delta\tau_{pot}(x)$ is positive so $G_{II}^s(x)$ increases and the slip event accelerates. After some propagation, small or negative $\Delta\tau_{pot}(x)$ leads to a decrease of $G_{II}^s(x)$ until $G_{II}^s(x) \leq \Gamma(x)$ and rupture terminates. These estimated locations of rupture termination are compared to those measured with slip sensors $E_1 - E_{16}$ (Figure 3d).

5. Results and Discussion

This work indicates that rupture termination is primarily controlled by $\Delta\tau_{pot}(x)$ (equation (5)) which is the stress on the fault in excess of the residual strength τ_r. $\Delta\tau_{pot} > 0$ indicates that the fault rocks are stressed to a level where, if triggered, a slip event could release some of the stored elastic strain energy and fuel the earthquake. This condition generally supports rupture propagation and is required for nucleation of a slip event. $\Delta\tau_{pot}(x) < 0$ inhibits slip events. However, negative $\Delta\tau_{pot}$ does not directly imply rupture termination; the arrest criterion is formulated in terms of energy (equation (1)). In our experiments, ruptures terminate by running out of available energy ($\Delta\tau_{pot} < 0$, which reduces G_{II}^s by orders of magnitude) rather than due to high Γ barriers (Bayart et al., 2018).

This work also shows that the LEFM-based model (Bayart et al., 2016; Kammer et al., 2015) originally developed for experimental observations on smaller PMMA samples is applicable to laboratory-generated earthquakes

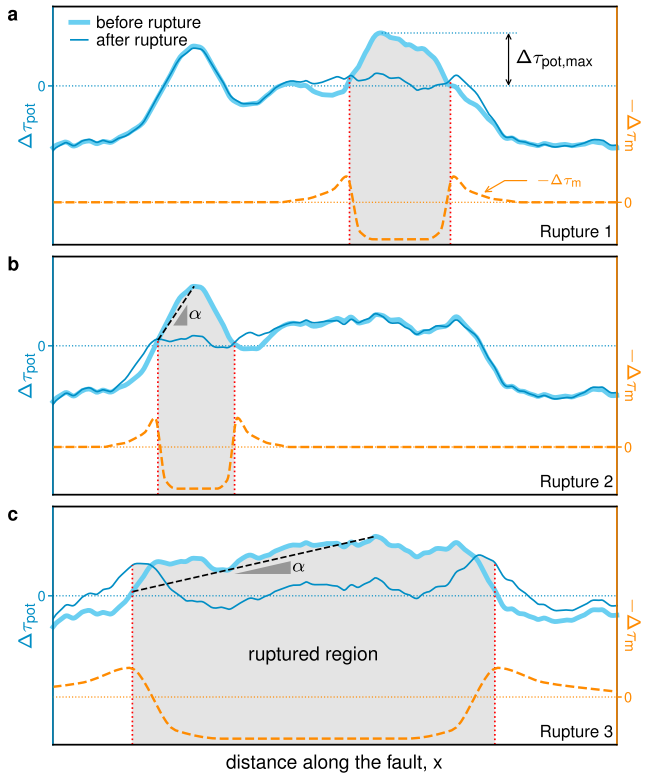

Figure 4. Schematic diagram of stress changes over a sequence of three hypothetical earthquakes. If rupture nucleates where $\Delta\tau_{pot} > 0$, the energy-based linear elastic fracture mechanics model determines rupture extent, assuming $\Gamma \approx$ constant. The rupture event causes stress changes $-\Delta\tau_m$, shown in orange. Stress is reduced within the ruptured region, but increases in surrounding areas, consistent with our observations. Continued tectonic loading increases, $\Delta\tau_{pot}$ until rupture initiates again. Rupture extent is primarily controlled by the average slope α of $\Delta\tau_{pot}$, near $\Delta\tau_{pot,max} = \max(\Delta\tau_{pot}(x))$. Our experiments show how smaller events (a and b) can smooth $\Delta\tau_{pot}(x)$ to prepare the fault for a larger event (c).

independent of size and material. We have also extended the method to include bilateral ruptures where nucleation is not affected by edge effects and more closely resembles scenarios expected for natural earthquakes. Our estimated $\gamma = 0.2\,\mu m$ (equation (7)) is similar to $\gamma = 0.28–0.35\,\mu m$ derived form a PMMA experiment at similar stress levels (Bayart et al., 2016). This, and the overall similarity between rupture sequences observed on the 3.1-m rock and smaller PMMA samples, shows that friction properties are similar enough between the two materials to validate the use of PMMA as a suitable analog for a larger rock sample, at least for rupture termination studies. This suitability may not extend to earthquake nucleation, where a strong sensitivity to details of the friction behavior has been shown (Ampuero & Rubin, 2008; Uenishi & Rice, 2003).

To compare γ to other studies, we utilize the linear slip-weakening friction relation (Andrews, 1976; Palmer & Rice, 1973) where $\gamma = D_c\Delta\mu/2$. Assuming a characteristic weakening length $D_c = 1\,\mu m$, common for bare granite surfaces (Mclaskey & Yamashita, 2017), we estimate $\Delta\mu = \Delta\tau/\sigma = 0.4$. This is consistent with frictional weakening from flash heating reported in high-speed rock friction experiments (Di Toro et al., 2011) with slip rates of $10^{-3}–10^{-1}$ m/s. Such experiments (Nielsen et al., 2016) also show that weakening continues (τ_f drops further) even after a meter of fault slip. This suggests that Γ increases with increasing slip and increasing earthquake magnitude, consistent with scaling behavior observed from seismic observations (Abercrombie & Rice, 2005; Viesca & Garagash, 2015). Given the small size (**M** −2.5) of our events, our estimation, $\Gamma \approx 0.1 – 4\,J/m^2$, is consistent with seismological trends (Viesca & Garagash, 2015), but if $\Gamma(x) = \gamma\sigma_0(x)$ scaling holds, then when scaled to stress levels expected in the upper crust, our γ estimate would predict higher Γ than those inferred from **M** −2.5 earthquakes recorded in deep boreholes. However, in our experiments, smaller modeled γ still leads to reasonable rupture length estimations (Figure 3f for $\gamma < 0.01\,\mu m$). The upper bound on γ is stronger since higher fracture energy would suppress dynamic ruptures entirely.

Relevant parameters such as $\Delta\tau_{pot}$ and Γ are essentially immeasurable at depth, but may be deduced from observations of seismic sequences (Jiang & Lapusta, 2016; Veedu & Barbot, 2016) if the underlying mechanics are known. Our experimental setup and modeling framework provide a link between stress conditions, small-scale friction properties (e.g., γ), and larger-scale seismic observations. For example, Figure 4 depicts the expected evolution of $\Delta\tau_{pot}(x)$ over a sequence of earthquakes. $\Delta\tau_{pot}(x)$ is difficult to measure because it is a function of residual frictional strength $\tau_r(x)$ which likely depends on slip (as described above), slip rate, and slip time history, but since its maximum $\Delta\tau_{pot,\,max}$ is limited, the average slope α of $\Delta\tau_{pot}$, principally affects rupture extent. Shallow slopes can support large areas of positive $\Delta\tau_{pot}$, and thus large earthquakes (Figure 4c).

In our experiments, small events do little to relieve stress or reduce the danger of a larger quake. Rather, they reorganize stress to allow for larger, complete-rupture events, in agreement with previous work, for example, Carlson and Langer (1989). This smoothing process may, in natural faults, compete with other mechanisms that produce or maintain heterogeneous stress fields (Aagaard & Heaton, 2008). During a small event, stress is reduced within the rupture area but increases in adjacent regions (as shown in Figures 3b and 4). These stress changes flatten the peaks of $\Delta\tau_{pot}(x)$ and ripen the fault for a larger subsequent event. The small events we sometimes observe between two complete-rupture events only occur at the end of the fault where we are applying a load and are thus introducing nonuniform stress through continued loading. Events of this type are never observed when stress is applied more uniformly as in McLaskey et al. (2015).

The success of the LEFM model and the similarity of the observed behavior to that of smaller, plastic samples may be limited to cases with a clearly defined fault and minimal off-fault damage, which could add compliance to the fault zone and reflect energy back into the rupturing fault. Larger earthquakes that occur on rougher faults, especially those that rupture multiple fault segments, may also require the consideration of high strength barriers and some modifications to our idealized formulation.

6. Conclusions

Our large-scale experiments generate realistic laboratory earthquakes by allowing ruptures to nucleate, propagate, and terminate within 3 m of crustal rock. The **M** −2.5 events do not rupture through the ends of the 3-m rock/rock fault and have a slip distribution that varies along the fault (Figure 3d), and these qualities make them more similar to natural earthquakes than standard stick-slip events that rupture the entire sample. Through LEFM, we showed how the balance between energy release rate and fracture energy governs the termination of a rupture. In our experiments $\Gamma(x)$ is essentially constant compared to the orders-of-magnitude variations in $G^s_{II}(x)$ (Figure 3c) so ruptures terminate because they run out of available strain energy. The utility of the model for both 3-m rock experiments and 200-mm PMMA experiments, and the similarity of fracture energy coefficient γ between the two materials, verifies the adequacy of PMMA as an analog to crustal rock in this context. Finally, the LEFM-based model provides a framework for linking friction properties and on-fault stress conditions to observable earthquake sequences.

Acknowledgments
The authors thank Tim Bond, Bill Wu, Anthony Reid, Don McLaskey, and Tim Brock for assistance constructing the 3-m machine. The authors thank Roland Bürgmann and Ilya Svetlizky for comments on the manuscript and Ze'ev Reches and an anonymous reviewer for their constructive reviews. Funding: This research was supported by USGS Earthquake hazards grant G18AP00010. Authors contributions: D.S.K. and G.C.M. designed this study. G.C.M. designed the experimental apparatus. C.-Y.K. and G.C.M. performed the measurements. C.-Y.K. and D.S.K. performed LEFM analysis. All authors contributed to the analysis and writing the manuscript. Competing interests: The authors declare that they have no competing interests. Data and materials availability: All data needed to evaluate the conclusions in the paper are present in the paper and/or the supporting information.

References

Aagaard, B. T., & Heaton, T. H. (2008). Constraining fault constitutive behavior with slip and stress heterogeneity. *Journal of Geophysical Research*, *113*, B04301. https://doi.org/10.1029/2006JB004793

Abercrombie, R. E., & Rice, J. R. (2005). Can observations of earthquake scaling constrain slip weakening? *Geophysical Journal International*, *162*(2), 406–424. https://doi.org/10.1111/j.1365-246X.2005.02579.x

Ampuero, J. P., & Rubin, A. M. (2008). Earthquake nucleation on rate and state faults—Aging and slip laws. *Journal of Geophysical Research*, *113*, B01302. https://doi.org/10.1029/2007JB005082

Andrews, D. J. (1976). Rupture propagation with nite stress in antiplane strain. *Journal of Geophysical Research*, *81*, 3575. https://doi.org/10.1029/JB081i020p03575

Bayart, E., Svetlizky, I., & Fineberg, J. (2016). Fracture mechanics determine the lengths of interface ruptures that mediate frictional motion. *Nature Physics*, *12*(2), 166–170. https://doi.org/10.1038/nphys3539

Bayart, E., Svetlizky, I., & Fineberg, J. (2018). Rupture dynamics of heterogeneous frictional interfaces. *Journal of Geophysical Research: Solid Earth*, *123*, 3828–3848. https://doi.org/10.1002/2018JB015509

Ben-David, O., Rubinstein, S. M., & Fineberg, J. (2010). Slip-stick and the evolution of frictional strength. *Nature*, *463*(7277), 76–79. https://doi.org/10.1038/nature08676

Carlson, J. M., & Langer, J. S. (1989). Properties of earthquakes generated by fault dynamics. *Physical Review Letters*, *62*(22), 2632–2635. https://doi.org/10.1103/PhysRevLett.62.2632

Chang, J. C., Lockner, D. A., & Reches, Z. (2012). Rapid acceleration leads to rapid weakening in earthquake-like laboratory experiments. *Science*, *338*(6103), 101–105. https://doi.org/10.1126/science.1221195

Di Toro, G., Han, R., Hirose, T., De Paola, N., Nielsen, S., Mizoguchi, K., et al. (2011). Fault lubrication during earthquakes. *Nature*, *471*(7339), 494–498. https://doi.org/10.1038/nature09838

Dieterich, J. H. (1979). Modeling of rock friction: 1. Experimental results and constitutive equations. *Journal of Geophysical Research*, *84*, 2161. https://doi.org/10.1029/JB084iB05p02161

Freund, L. B. (1979). The mechanics of dynamic shear crack propagation. *Journal of Geophysical Research*, *84*, 2199. https://doi.org/10.1029/JB084iB05p02199

Harris, R. A., Barall, M., Archuleta, R., Dunham, E., Aagaard, B., Ampuero, J. P., et al. (2009). The SCEC/USGS dynamic earthquake rupture code verification exercise. *Seismological Research Letters*, *80*(1), 119–126. https://doi.org/10.1785/gssrl.80.1.119

Jiang, J., & Lapusta, N. (2016). Deeper penetration of large earthquakes on seismically quiescent faults. *Science*, *352*(6291), 1293–1297. https://doi.org/10.1126/science.aaf1496

Kammer, D. S., Radiguet, M., Ampuero, J.-P., & Molinari, J.-F. (2015). Linear elastic fracture mechanics predicts the propagation distance of frictional slip. *Tribology Letters*, *57*(3), 23. https://doi.org/10.1007/s11249-014-0451-8

Lockner, D. A., Okubo, P. G., & Dieterich, J. H. (1982). Containment of stick-slip failures on a simulated fault by pore fluid injection. *Geophysical Research Letters*, *9*(8), 801–804. https://doi.org/10.1029/GL009i008p00801

Maegawa, S., Suzuki, A., & Nakano, K. (2010). Precursors of global slip in a longitudinal line contact under non-uniform normal loading. *Tribology Letters*, *38*(3), 313–323. https://doi.org/10.1007/s11249-010-9611-7

Marone, C. (1998). Laboratory-derived friction laws and their application to seismic faulting. *Annual Review of Earth and Planetary Sciences*, *26*(1), 643–696. https://doi.org/10.1146/annurev.earth.26.1.643

McLaskey, G. C., Kilgore, B. D., & Beeler, N. M. (2015). Slip-pulse rupture behavior on a 2 m granite fault. *Geophysical Research Letters*, *42*, 7039–7045. https://doi.org/10.1002/2015GL065207

Mclaskey, G. C., & Yamashita, F. (2017). Slow and fast ruptures on a laboratory fault controlled by loading characteristics. *Journal of Geophysical Research: Solid Earth*, *122*, 3719–3738. https://doi.org/10.1002/2016JB013681

Nielsen, S., Spagnuolo, E., Smith, S. A. F., Violay, M., Di Toro, G., & Bistacchi, A. (2016). Scaling in natural and laboratory earthquakes. *Geophysical Research Letters*, *43*, 1504–1510. https://doi.org/10.1002/2015GL067490

Palmer, A. C., & Rice, J. R. (1973). The growth of slip surfaces in the progressive failure of over-consolidated clay. *Proceedings of the Royal Society A: Mathematical, Physical and Engineering Sciences*, *332*(1591), 527–548. https://doi.org/10.1098/rspa.1973.0040

Passelegue, F. X., Schubnel, A., Nielsen, S., Bhat, H. S., & Madariaga, R. (2013). From sub-Rayleigh to supershear ruptures during stick-slip experiments on crustal rocks. *Science*, *340*(6137), 1208–1211. https://doi.org/10.1126/science.1235637

Rubinstein, S. M., Cohen, G., & Fineberg, J. (2004). Detachment fronts and the onset of dynamic friction. *Nature*, *430*(7003), 1005–1009. https://doi.org/10.1038/nature02830

Rubinstein, S. M., Cohen, G., & Fineberg, J. (2007). Dynamics of precursors to frictional sliding. *Physical Review Letters*, *98*(22), 1–4. https://doi.org/10.1103/PhysRevLett.98.226103

Svetlizky, I., & Fineberg, J. (2014). Classical shear cracks drive the onset of dry frictional motion. *Nature*, *509*(7499), 205–208. https://doi.org/10.1038/nature13202

Svetlizky, I., Kammer, D. S., Bayart, E., Cohen, G., & Fineberg, J. (2017). Brittle fracture theory predicts the equation of motion of frictional rupture fronts. *Physical Review Letters*, *118*(12), 125501. https://doi.org/10.1103/PhysRevLett.118.125501

Tada, H., Paris, P. C., & Irwin, G. R. (2000). *The stress analysis of cracks handbook Edited by* 3. Three Park Avenue New York, NY 10016-5990: ASME. https://doi.org/10.1115/1.801535

Uenishi, K., & Rice, J. R. (2003). Universal nucleation length for slip-weakening rupture instability under nonuniform fault loading. *Journal of Geophysical Research*, *108*, 2042. https://doi.org/10.1029/2001JB001681

Veedu, D. M., & Barbot, S. (2016). The Parkfield tremors reveal slow and fast ruptures on the same asperity. *Nature*, *532*(7599), 361–365. https://doi.org/10.1038/nature17190

Viesca, R. C., & Garagash, D. I. (2015). Ubiquitous weakening of faults due to thermal pressurization. *Nature Geoscience*, *8*(11), 875–879. https://doi.org/10.1038/ngeo2554

Xia, K., Rosakis, A. J., Kanamori, H., & Rice, J. R. (2005). Laboratory earthquakes along inhomogeneous faults: Directionality and super shear. *Science*, *308*(April), 681–684. https://doi.org/10.1126/science.1108193